

A Bayesian Classifier for Photometric Redshifts: Identification of high redshift clusters

Tadayuki Kodama¹, Eric F. Bell² & Richard G. Bower²

¹ *Institute of Astronomy, University of Cambridge, Madingley Road, Cambridge CB3 0HA, UK*

² *Department of Physics, University of Durham, South Road, Durham DH1 3LE, UK*

5 October 1998

ABSTRACT

Photometric redshift classifiers provide a means of estimating galaxy redshifts from observations using a small number of broad-band filters. However, the accuracy with which redshifts can be determined is sensitive to the star formation history of the galaxy, for example the effects of age, metallicity and on-going star formation. We present a photometric classifier that explicitly takes into account the degeneracies implied by these variations, based on the flexible stellar population synthesis code of Kodama & Arimoto. The situation is encouraging since many of the variations in stellar populations introduce colour changes that are degenerate. We use a Bayesian inversion scheme to estimate the likely range of redshifts compatible with the observed colours. When applied to existing multi-band photometry for Abell 370, most of the cluster members are correctly recovered with little field contamination. The inverter is focussed on the recovery of a wide variety of galaxy populations in distant ($z \sim 1$) clusters from broad band colours covering the 4000 Å break. It is found that this can be achieved with impressive accuracy ($|\Delta z| < 0.1$), allowing detailed investigation into the evolution of cluster galaxies with little selection bias.

Key words: galaxies: general – galaxies: evolution – galaxies: stellar content

1 INTRODUCTION

The current trend in cosmology is to explore the properties of galaxies at ever fainter limits. This has led to demonstration of the existence of a substantial galaxy population at $z > 3$ (Steidel et al. 1996, Metcalfe et al. 1996, Steidel et al. 1998), and the discovery of galaxy clusters with $z \gtrsim 1$ (Deltorn et al. 1997, Stanford et al. 1997, Yamada et al. 1997). These discoveries have allowed us to extend our knowledge of the formation history of galaxies (Madau et al. 1996, Baugh et al. 1998, Kodama et al. 1998) and the growth of the universe’s gravitational structure (Bower & Smail 1997). However, while images that reach these depths are now relatively commonplace, spectroscopic follow-up of these objects is extremely time consuming even on 8m-class telescopes. These problems are offset by the multiplex capability of multi-object spectrographs (eg. LDSS; Allington-Smith et al. 1994) and fibre-optic fed spectrographs (eg. Taylor 1995), or by surveys targeted at specific redshifts using tuneable narrow-band filters (eg. Jones & Bland-Hawthorn 1997). Nevertheless, even in the best studied deep images, only a small fraction of the galaxies have known spectroscopic redshifts.

Whereas spectroscopic redshifts use sharp absorption and/or emission lines to accurately determine the rest wave-

length of the spectrum, it is also possible to exploit the overall characteristic shape of the spectral energy distribution (SED) to estimate the galaxy’s redshift. This ‘photometric redshift’ approach can be applied to broad band images provided they have sufficiently high signal to noise and adequately sample the important features of the SED. In particular, the 4000 Å spectral break and the Balmer and Lyman series limits are important features that arise in almost all galaxy spectra. Although precise redshifts cannot be determined by this method, estimates of (or limits on) z are obtained.

The existing photometric redshift estimators fall into three main classes: empirical redshift estimators, those based on observed spectral energy distributions and model-based redshift estimators. Empirical redshift estimators (Connolly et al. 1995) are based on a training set of galaxies for which the redshifts and broad-band fluxes are known. These are used to train an estimator, for example a multi-dimensional polynomial fit, that predicts the redshift from the input fluxes with minimum error. The disadvantage of this method is that it requires a relatively large training dataset with high quality colours and known redshifts. This makes it difficult to apply beyond the limits of spectroscopic surveys, although this problem might be alleviated using the colours of distant, gravitationally lensed galaxies. However

arXiv:astro-ph/9806120v3 9 Oct 1998

this method, when tested against independent but similar data, can give impressive accuracy ($\sigma_z \sim 0.06$; Connolly et al. 1995).

Lanzetta et al. (1996), Mobasher et al. (1996) and Sawicki et al. (1997) use an approach that is based on the observed SEDs of galaxies covering a wide range of spectral types. Redshifts are estimated from the observed data by redshifting each of the templates and determining the best match to the observational colours. They emphasise the importance of using observed templates in order to incorporate the effects of dust. This is particularly important for galaxies in the redshift range $1 < z < 3$ because the optical colours increasingly reflect the rest frame ultraviolet spectrum of the galaxy. One problem with this approach, however, is that the spectral library does not take into account the evolution of the galaxy stellar populations. The method can accommodate evolution in as far as it is equivalent to changing galaxies between different spectral types, however.

Model-based approaches use stellar population synthesis codes (eg. Bruzual & Charlot 1993) to produce model SEDs that can then be compared to the observed data. For example, Gwyn & Hartwick (1996) used a spread of galaxy models from single burst stellar populations to models with constant star formation to model present-day galaxies. When generating redshifted model SEDs, the evolution of the stellar population is automatically taken into account. The redshift of the observed galaxy is determined by minimising χ^2 residuals. The improved flexibility of this method can however, lead to greater errors in the estimated redshifts. This arises because of colour degeneracies between the effects of galaxy type and redshift.

In this paper, we focus more closely on the interrelation between star formation history and redshift estimation. As we have outlined, photometric redshifts can be susceptible to changes in the galaxy stellar population. For instance, the effects of age, metal abundance and on-going star formation are all reflected in the relative shape of the continuum, particularly when it is convolved with the response of standard broad band filters. It is important that these uncertainties are taken into account when determining the galaxy redshift. We develop a method of photometric redshift determination that explicitly takes into account the degeneracies implied by these variations. Clearly, incorporating additional free parameters to describe the star formation history of the galaxy threatens to make it impossible to extract useful redshift information. However, many of the changes in colour caused by different star formation histories are degenerate: this is the familiar age-metallicity degeneracy that has long plagued the estimation of star formation histories in elliptical galaxies. We will show that for red galaxies, redshifts can be determined under only weak assumptions about the star formation history. At lower redshifts, the colours of blue (disk) galaxies become considerably harder to disentangle.

Our approach attempts to deal with, and indeed embrace, this unavoidable degeneracy in colours with variations in redshift and star formation history. We explicitly account for galaxy metallicities and star formation histories; these effects are in many cases degenerate with uncertainties due to the stellar initial mass function (IMF), recent star formation, dust extinction and cosmology. We retain possible degeneracies in plausible values of galaxy type and redshift by storing a ‘probability map’ for each galaxy, which can be

used to estimate a range of acceptable redshifts rather than reducing the observed data to a single ‘best bet’ estimate of galaxy type and redshift. In particular, our classifier is designed to pick out galaxy cluster members without biasing the sample to galaxies of one particular star formation history. Our motivation is to use this method to study the *photometric* properties of $z \sim 1$ cluster galaxies with as little selection bias as possible.

The structure of the paper is as follows. § 2 introduces the stellar population synthesis code of Kodama & Arimoto (1997). We derive colour tracks for a range of galaxy star formation histories and outline the major uncertainties in these tracks. This provides the framework for selecting appropriate filter sets and required photometric accuracy. § 3 details our Bayesian approach to the inversion problem. We explicitly incorporate a wide variety of possible star formation histories, and explicitly incorporate the resulting degeneracies in our redshift estimates. The role of the prior is discussed. In § 4, we test our method with galaxies in Abell 370 cluster field and galaxies with known redshifts in the Hubble Deep Field (HDF). § 5 gives an application of the method to a simulated cluster at $z = 1$. A summary and our conclusions are presented in § 6.

2 COLOUR TRACKS AS A FUNCTION OF STAR FORMATION HISTORY

2.1 Model

The evolutionary population synthesis model of Kodama (1997) was used to predict the photometric properties of evolving stellar populations. This model calculates the spectral evolution of a galaxy with an arbitrary star formation history, taking into account the chemical evolution in a self-consistent way. Kodama & Arimoto (1997) applied this model to the elliptical galaxy populations of distant clusters. In this study, disk models with ongoing star formation are considered in addition to the elliptical models. We first describe the basic equations and parameters of this model and then summarise the elliptical galaxy and disk galaxy models.

2.1.1 Equations and parameters

We assume that the galactic gas is supplied from a surrounding gas reservoir trapped in the gravitational potential of a galaxy and that the gas is always well-mixed and distributes uniformly in a galaxy. The star formation is described by the following equations. The stellar IMF is given by a single power law:

$$\phi(m) = Am^{-x}, \quad m_l \leq m \leq m_u, \quad (1)$$

where m_l and m_u are lower and upper limits of initial stellar mass respectively. The Salpeter (1955) IMF corresponds to $x = 1.35$. The coefficient A is determined by,

$$\int_{m_l}^{m_u} \phi(m) dm = 1. \quad (2)$$

The IMF is assumed to be time invariant. The star formation rate (SFR) $\psi(t)$ is assumed to be proportional to the gas mass $M_g(t)$ (Schmidt 1959):

$$\psi(t) = \frac{1}{\tau} M_g(t), \quad (3)$$

where τ is the star formation time scale in Gyr. Note that this formulation gives an exponentially decaying SFR with an effective time scale τ/α in the case of the simple models, where α is the so-called locked-up mass fraction defined by Tinsley (1980). The Salpeter mass function ($x = 1.35$) with $m_l = 0.1$, $m_u = 60 M_\odot$ gives $\alpha = 0.72$. The gas infall rate $\xi_{in}(t)$ depends on the initial total mass of the gas reservoir M_T and the gas infall time scale τ_{in} :

$$\xi_{in}(t) = \frac{M_T}{\tau_{in}} \exp\left(-\frac{t}{\tau_{in}}\right) \quad (4)$$

(cf. Köppen & Arimoto 1990). The gas metallicity $Z_g(t)$ is calculated numerically, using the basic equations of chemical evolution (Tinsley 1980) and stellar nucleosynthesis tables (Nomoto 1993). The metal contribution from SNIa is also considered by fixing their lifetime at 1.5 Gyr. We assume that the metal-enriched gas spreads through the galaxy instantaneously and evenly (the one-zone approximation). As the initial conditions, we assume that there is no gas in a galaxy before the onset of star formation; ie. $M_g(0) = 0$ and $Z_g(0) = 0$. Using the infall history defined as above, our expression for the star formation rate $\psi(t)$ and the metallicity of the stars $Z(t) = Z_g(t)$, the integrated spectrum of a galaxy can be synthesised as a function of time. By specifying the galaxy age, or equivalently its formation redshift, and cosmological parameters, we obtain the spectra and therefore colour indices of the galaxy as a function of redshift. The cosmological parameters are set to $H_0 = 50 \text{ km s}^{-1} \text{ Mpc}^{-1}$, $\Omega_0 = 1.0$, and $\Lambda_0 = 0.0$ unless otherwise stated.

2.1.2 Elliptical galaxies and bulges

For elliptical galaxy models (E models), we use $x = 1.10$, $m_l = 0.1 M_\odot$, and $m_u = 60 M_\odot$ for the IMF and short time scales of star formation and gas infall: $\tau = \tau_{in} = 0.1 \text{ Gyr}$. The slope of the IMF differs from the Salpeter value $x = 1.35$ to allow the colours of the reddest giant ellipticals to be reproduced in the context of this model (with a Salpeter IMF, metallicities high enough cannot be achieved). In addition, in order to reproduce the observed present-day dependence of elliptical galaxy colour on luminosity, it is useful to introduce another parameter, the galactic wind epoch t_{gw} . At this time, the energy put into the ISM in the proto-elliptical galaxy by SNe is large enough to overcome the potential of the galaxy, resulting in the ejection of the gas from the galaxy, ending star formation. We constructed a model sequence of elliptical galaxies as a function of total luminosity by simply changing t_{gw} so that they reproduce the colour-magnitude ($C-M$) relation of Coma ellipticals in $V-K$ and $U-V$ (Bower, Lucey, & Ellis 1992a,b) at the galaxy age $T_G = 12 \text{ Gyr}$. Changing t_{gw} is equivalent to adjusting the mean stellar metallicity of the galaxies, therefore we call this the *metallicity sequence* of elliptical galaxy models. In this model, the mean stellar metallicity $\langle [M/H] \rangle$ changes from 0.06 to -0.52 over a six magnitude range from the brightest E model ($M_V = -23 \text{ mag}$ at $z = 0$). The time until the onset of a galactic wind t_{gw} is always shorter than $\sim 0.5 \text{ Gyr}$, thus the star formation in elliptical galaxies is burst-like. The above model sequence is shown to reproduce the

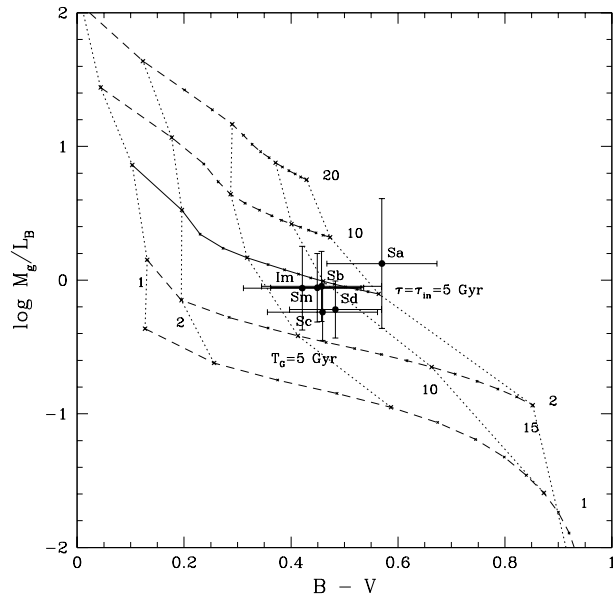


Figure 1. Galaxy disks. Gas mass per unit blue luminosity is plotted against $B-V$ colours. The filled circles show the estimated disk colours of galaxies ranging between Sa and Im (see text). The solid line and the four dashed line represent the evolutionary models with different τ and τ_{in} . The age T_G is changed from 1 Gyr to 15 Gyr as indicated by crosses along the lines.

evolution of the $C-M$ relation of elliptical galaxies in distant clusters in Kodama & Arimoto (1997) and Kodama et al. (1998).

To represent the photometric properties of disk galaxy bulges, we borrow the elliptical galaxy models. Observational support for this includes the results of Mg_2 index analysis (Jablonka, Martin, & Arimoto 1996).

2.1.3 Disks

For the disk component, the IMF parameters are set to $x = 1.35$, $m_l = 0.1$, $m_u = 60 M_\odot$, and longer time scales of star formation and gas infall: $\tau = \tau_{in} = 5 \text{ Gyr}$. The age of a galactic disk is fixed at 12 Gyr. The disk model time scales are chosen to reproduce the integrated $B-V$ colours and M_g/L_B ratio of observed disks of various Hubble-types as shown in Fig. 1 (cf. Shimasaku & Fukugita 1997).

The $B-V$ colours of disks shown in Fig. 1 as a function of Hubble type are estimated from:

- the mean total $B-V$ colours as a function of Hubble type (Buta et al. 1994), and
- subtraction of the bulge light by assuming a bulge colour $B-V = 1.0$ and a bulge to total light ratio (B/T) in B -band (Simien & de Vaucouleurs 1986).

The total gas masses normalised by B -band disk luminosity (M_g/L_B) as a function of Hubble type are estimated from:

- the mass of neutral atomic gas, calculated from the integrated hydrogen index H α (Buta et al. 1994) and a conversion formula in *Third Reference Catalogue of Bright Galaxies* (RC3) given by de Vaucouleurs et al. (1991),

Table 1. Integrated colours of spiral galaxies.

Hubble type	de Jong (1996)						RC3				Model			
	B/T	B–V	V–R	V–I	V–K	U–V	B–V	V–R	V–I	U–V	B–V	V–R	V–I	V–K
Sa	0.41	0.81	0.54	1.02	2.94	0.96	0.74	0.50	1.14	0.85	0.76	0.53	1.17	3.02
Sb	0.24	0.74	0.46	1.04	2.79	0.66	0.61	0.46	0.93	0.63	0.66	0.49	1.07	2.84
Sc	0.09	0.67	0.53	1.08	2.84	0.45	0.53	0.41	0.87	0.45	0.57	0.43	0.95	2.61
Sd	0.02	0.59	0.47	1.02	2.59	0.37	0.50	0.39	0.83	0.36	0.52	0.41	0.89	2.47
Sm	0.00	0.69	0.41	0.75	2.30	0.33	0.50	0.36	0.72	0.33	0.50	0.40	0.87	2.42

- the ratio of molecular to atomic gas H_2/HI (Young & Knezek 1989),
- a helium abundance correction of 25%, and
- subtraction of the bulge light contribution to L_B .

Disk properties in Fig. 1 are well reproduced by $\tau = \tau_{in} = 5$ Gyr model with an age $T_G = 5 - 15$ Gyr irrespective of the Hubble type. The model also reproduces the age-metallicity relation and the $[O/Fe]$ vs. $[Fe/H]$ diagram of the stars in our own galaxy (Kodama 1997). The constraint on the time scales τ and τ_{in} is weak because of the large observational errors and the permitted range could be from 2 to 8 Gyr (Fig. 1). However, as will be shown in the next section (§ 2.2), this uncertainty will not cause problems for the purposes of redshift determination because star forming timescale and B/T variations have degenerate effects.

As an additional check of the validity of our models, the integrated colours of disk galaxies of different Hubble type are compared in Table 1. The observational data are mean Hubble type colours taken from de Jong (1996) and the RC3 (Buta et al. 1994; Buta & Williams 1995). Note that each galaxy type has large intrinsic colour dispersion, typically as much as 0.05 – 0.2 mag in optical colours and 0.2 – 0.4 mag in $V - K$. The data are compared to the model with appropriate B -band B/T ratio (Simien & de Vaucouleurs 1986). It is clear that the detailed trends of local galaxy colour with B -band B/T ratio are well reproduced by our models.

2.2 Colour tracks

Following the models introduced above, we simulate the colour evolution of galaxies as a function of redshift for variety of star formation histories.

The two solid curves in Fig. 2 show the colour evolution in the observer’s frame for a E model with a high metallicity ($\langle[M/H]\rangle=0.06$), and a model which contains 50% contribution of disk light in the B -band at $z = 0$ (see below). The redshift is changed from 0 to 2 in steps of 0.05 as indicated by the dots along the lines. Four different colour-colour plots are shown, to cover a wide range in redshift, demonstrating that the most useful passbands for photometric redshift determination up to redshifts of ~ 1.5 typically bracket the 4000 Å break: $0.25 \leq z \leq 0.4$ for $B - V$ vs. $V - R$ colours, $0.5 \leq z \leq 0.8$ for $V - R$ vs. $R - I$ colours, $0.9 \leq z \leq 1.15$ for $R - I$ vs. $I - K$ colours, and $1.0 \leq z \leq 1.5$ for $R - Z$ vs. $Z - J$ colours. In the above redshift ranges, the middle bands of each combination are passing through 4000 Å break, the most prominent spectral feature in optical re-

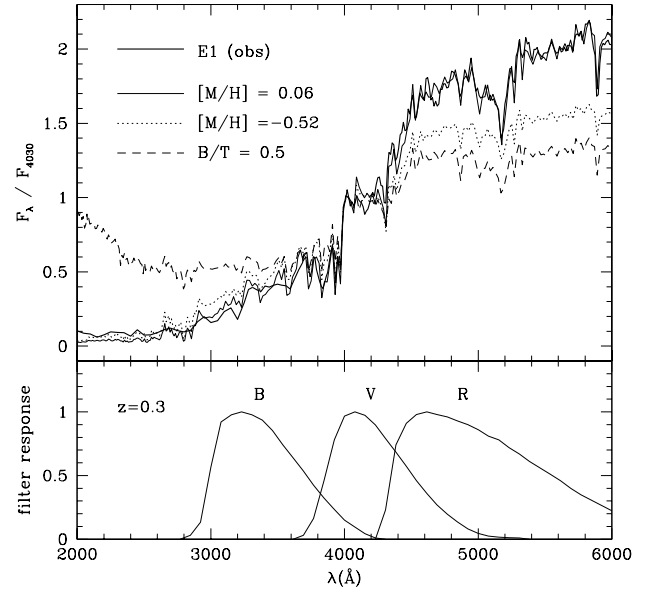


Figure 3. The galaxy spectra at $z = 0$ (upper panel). The flux is normalised at 4030 Å. The thick solid line shows a giant elliptical E1 spectral template (Bica 1988) extended into the UV by the attachment of IUE spectra (Arimoto 1996). Three model spectra are superposed: a high mean metallicity model with $\langle[M/H]\rangle = 0.06$ (thin solid line), a lower metallicity model with $\langle[M/H]\rangle = -0.52$ (dotted line), and a high metallicity bulge plus disk model with $B/T=0.5$ (dashed line). See text for details of the models. The lower panel shows the normalised response functions of standard Johnson-Cousins’ B, V and R filters, blueshifted to correspond to those at $z = 0.3$.

gion, which plays an important role in redshift estimation. The horizontal colours redden rapidly with redshift while vertical colours stay nearly constant. At around $z = 0.3$ for example, as shown in Fig. 3, V band is just on the 4000 Å break and B and V bands are losing flux rapidly, while the R band flux is approximately constant as the redshift increases. As a result $V - R$ gets redder while $B - V$ remains almost constant. On the other hand, $B - V$ is more sensitive to changes in stellar population than $V - R$. Therefore, we can see that the effects caused by changes in redshift are almost perpendicular to those caused by changes in star formation history.

In Fig. 2, six possible effects which change the colour

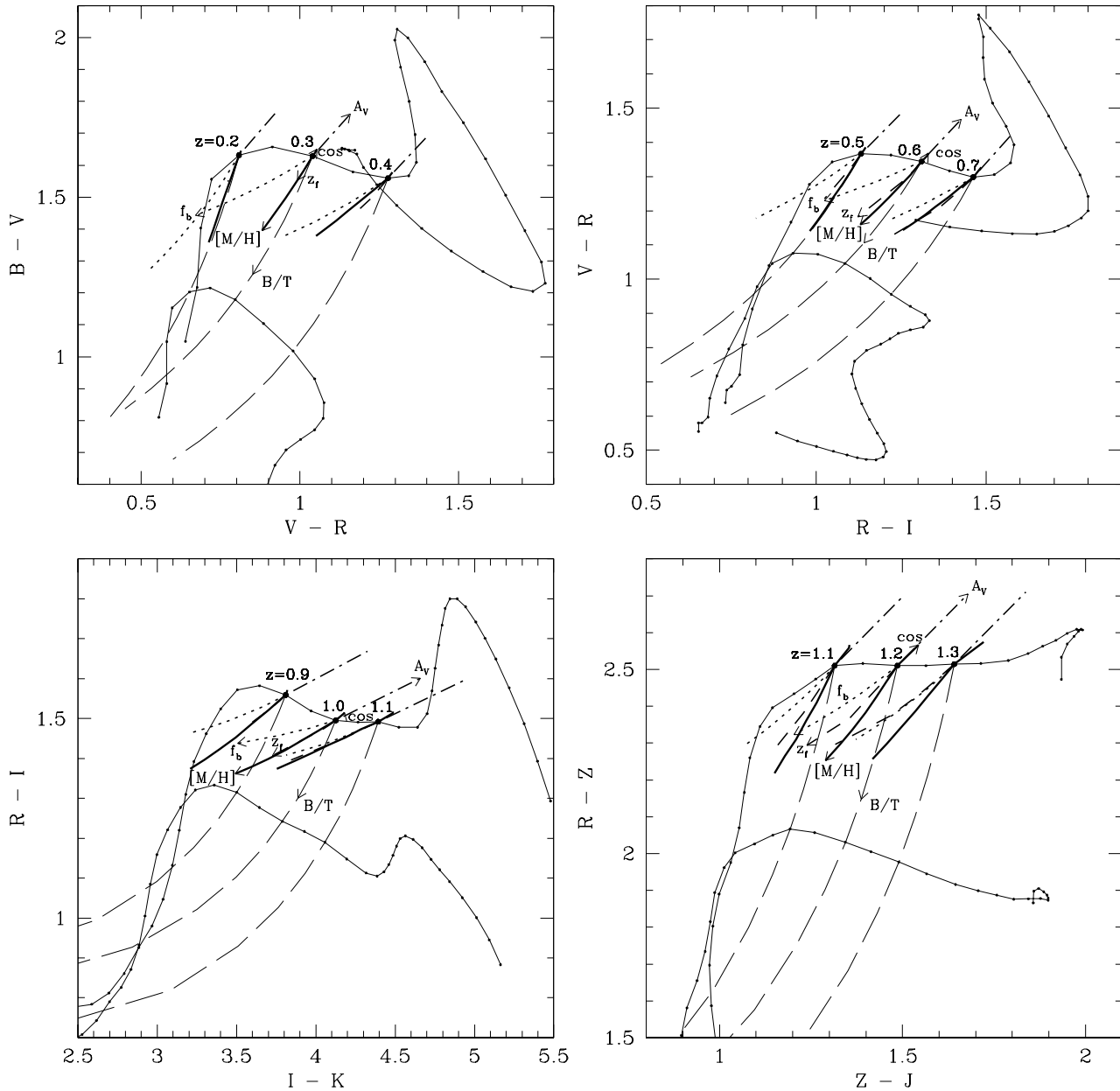


Figure 2. Colour-colour plots in the observer’s frame. The two solid curves show the colour evolution of an old ($T_G = 12$ Gyr, or $z_f = 4.5$), high metallicity ($\langle[M/H]\rangle=0.06$) E model (redder), and the B/T=0.5 model (bluer) which contains half of disk light in B-band at $z = 0$. The redshift is changing from 0 to 2 in steps of 0.05, indicated by dots along the tracks. The six arrows shown from three redshift points along the track indicate the colour changes due to several different effects. See text for detail.

evolution of a galaxy with redshift are considered. The six arrows (indicated at three redshift points along the colour track) show the change in colour of an old, high metallicity elliptical model ($T_G = 12$ Gyr and $\langle[M/H]\rangle=0.06$) caused by the following effects.

(i) *metallicity* — *lower thick solid arrows*: The mean stellar metallicity of the E models is changed from

$\langle[M/H]\rangle=0.06$ to -0.52 . The galaxy age is fixed at 12 Gyr, corresponding to a formation redshift $z_f = 4.5$.

(ii) *age* — *dashed arrows*: The formation redshift of the E model is varied from $z_f = 4.5$ to 1.0 (4.5 to 2.0 for the *RIK* and *RZJ* diagrams), corresponding to galaxy ages $T_G = 12.0$ to 8.4 Gyr (12.0 to 10.5 Gyr). Metallicity is fixed at $\langle[M/H]\rangle=0.06$.

(iii) *disk component* — *long dashed arrows*: As outlined earlier, the models deal with disk galaxies by adding a star

forming disk component onto an E model, representing the galaxy bulge. The B -band B/T ratio at $z = 0$ is changed from 100% to 0%. Note that B/T=0.41, 0.24 and 0.09 corresponds to the Hubble types Sa, Sb and Sc, respectively (Simien & de Vaucouleurs 1986). Note also that B/T ratio is a rising function with redshift, since the bulge is getting brighter with redshift while the disk brightness remains roughly constant up to $z = 1$. For example, the B/T ratio of 0.5 at $z = 0$ actually increases to 0.8 at $z = 1$. We have also modelled the B/T sequence using $[M/H]_{\text{disk}} = -1.3$ and $[M/H]_{\text{disk}} = 0$ by forcing all the disk stars to have the same metallicity instead of following the chemical evolution of the disk. $[M/H]_{\text{disk}}$ is found to have a negligible effect on the colour tracks of the B/T sequence, and is not considered hereafter. The time scales τ and τ_{in} can be also changed, but it is found to be similar in effect to changes in B/T ratio at fixed τ and τ_{in} . This is because the colour of the B/T sequence at a given redshift is essentially determined by the ratio of the current star formation rate and the total mass of the galaxy. This parameter can be adjusted either by changing the time scales of the disk or by changing the B/T ratio. Thus the effects on the colour-colour diagrams of changing the timescales is only to shorten or extend the vectors of the B/T sequence for a given B/T ratio.

(iv) *recent star burst — dotted arrows*: The possible effects of recent large-scale star formation are considered by the addition of a recent star burst to the E model. The burst population is assumed to be a simple stellar population (SSP) with solar metallicity. The arrow denotes the changes caused by a $T_b = 0.5$ Gyr old burst population corresponding to 10% of the total stellar mass ($f_b = 0.1$) at that redshift. The direction of the vector on the colour-colour diagrams depends on T_b , but unless T_b is around 0.5 (± 0.3) Gyr, the burst sequence follows either the B/T sequence or the age sequence closely. Main-sequence turn-off stars in the burst population with age ~ 0.5 Gyr have an effective temperature of about 10000 K and contribute significantly to the total flux at rest wavelengths of 3000-4000 Å, creating aberrant colour changes in the colour-colour plots.

(v) *reddening — dash-dotted arrows*: The extinction effect due to internal dust is estimated by using the extinction curve given by Mathis (1990). The full arrows correspond to $A_V = 0.5$ mag.

(vi) *cosmology — upper thick solid arrows*: The colour tracks have a weak dependence on the adopted cosmology. Other sets of cosmological parameters are tested; ie. $H_0 = 65, \Omega_0 = 0.1, \Lambda_0 = 0.0$, and $H_0 = 80, \Omega_0 = 0.2, \Lambda_0 = 0.8$. The formation redshift z_f is fixed to 4.5 in all cases. The full arrows show the colour change for the latter cosmology. The colour change from the former cosmology is smaller and along a similar vector.

The age and metallicity sequences (i) and (ii) are almost indistinguishable in all the colour-colour plots for ages $\gtrsim 1$ Gyr. This reflects the age-metallicity degeneracy inherent in old stellar populations (Worthey 1994). However, this degeneracy actually improves the prospects for the determination of photometric redshifts, as the effects of age and metallicity are quite distinct, given the right choice of passbands, to the effects of changing galaxy redshift. In addition, it is clear from Fig. 2 that changes in assumed cosmology and interstellar reddening also have colour effects

similar to age and metallicity, with an opposite sense. As a result, E-type galaxies at a given redshift should populate in a restricted area on the colour-colour diagram (almost a single line) characteristic of that redshift, irrespective of its stellar population, regardless of interstellar reddening, and whichever cosmology is assumed. This means that it is possible to assign redshifts to old stellar populations without prior knowledge of galaxy properties.

However, the colour changes caused by the B/T sequence (iii) are not entirely degenerate with those due to age and metallicity on the RIK and RZJ diagrams (Fig. 2), due to the presence of on-going star formation. This on-going star formation causes a bluer eg. $R - I$ colour for a given $I - K$ colour than either the effects of age and metallicity for $z \sim 1$ galaxies. Recent large bursts of star formation of age ~ 0.5 Gyr (iv) also lead to effects distinct from those of age and metallicity, and those of changing the B/T ratio.

This can lead to considerable uncertainty in the estimation of galaxy redshift, as a given set of colours, on the basis of the colour-colour plots presented in Fig. 2, will be consistent with a wide range of redshifts, depending on how the colours are explained by our model; eg. by changing the B/T ratio, or the metallicity of the galaxy template. However, if a passband with a short rest-frame wavelength is used, it is possible to discriminate the presence of young stellar populations photometrically, leading to a less ambiguous determination of redshift, and some information on the star formation history of the galaxy. This is illustrated in the upper half of Table 2 (see also the lower left panel of Fig. 2), where we compare 3 galaxy templates with very similar red colours ($R - I \simeq 1.35, I - K \simeq 3.48$) which present very distinct colours in bluer passbands, allowing relatively easy discrimination between these possibilities. Another degeneracy apparent in Fig. 2 in redder passbands is that between high redshift, low B/T ratio galaxies, and lower redshift early-type galaxies. This, again, is illustrated in the lower half of Table 2 where we again see that bluer passbands allow easy splitting of this degeneracy.

Another point to note from Fig. 2 is that when a particular colour pair is selected to allow the accurate estimation of redshifts within a certain redshift range, this colour pair also provides a means of rejecting galaxies (particularly higher B/T objects) that lie outside this optimal redshift range (although the estimated redshifts will obviously be much less accurate for these objects). Problems will occur for much higher redshift objects, and objects with a small B/T ratio, as discussed above.

Despite the demonstrated utility of the bluer passbands in ‘breaking’ degeneracies between galaxies which look identical in red passbands, we aim to use little of the colour information shortwards of 2500 Å. Primarily, this is because the model spectra are ill-constrained for short UV wavelengths in both elliptical and star forming galaxies because of the effects of the UV-upturn (an anomalous rise in flux towards short UV wavelengths, observed in nearby giant ellipticals; eg., Burstein et al. 1988) and the uncertain effects of dust extinction (White, Keel, & Conselice 1996). The source of the UV-upturn is still poorly understood, and the model predictions for its source and effects are still uncertain. If the UV-upturn comes from hot young stars, this population is actually considered in this model by superposing only a small fraction of on-going star formation onto the passively

Table 2. Colour degeneracies.

z	B/T	$\langle[M/H]\rangle$	$f_b(\%)$	$B - R$	$V - R$	$R - I$	$I - K$
0.9	0.5	0.06	0	1.32	0.86	1.32	3.50
1.0	1.0	-0.52	0	2.57	1.32	1.36	3.49
1.1	1.0	0.06	20	1.64	1.09	1.38	3.46
0.5	1.0	0.06	0	2.98	1.37	1.13	3.10
0.7	0.4	0.06	0	1.48	0.89	1.15	2.98
0.9	0.2	0.06	0	0.80	0.57	1.09	3.00

evolving ellipticals. If, however, the source of the UV-upturn is hot horizontal branch stars, then it is necessary to fine tune the mass loss parameter along the red giant branch to reproduce the UV-upturn (cf. Yi, Demarque, & Oemler, 1997). Even if this were the case, such hot horizontal branch stars would disappear at high redshift ($z \gtrsim 1$), which is our main region of interest, since the envelope mass of a horizontal branch star gets larger as the mass of a main sequence turn off star gets larger with look back time.

An additional source of uncertainty in our models, especially in the UV, is the neglect of the effects of dust extinction on the colours of the stellar populations incorporating on-going star formation. This would at first appear to be a serious handicap, as disk-dominated galaxies clearly contain significant amounts of dust, especially in the spiral arms, where B band extinction $A_B \sim 1$ mag (White, Keel, & Conzelmann 1996, Berlind et al. 1997). However, by inspection of Fig. 2, it is clear that the colour changes at rest-frame optical wavelengths are equivalent to increasing B/T ratio, age or metallicity, meaning that relatively large uncertainties in dust reddening can be accommodated by changes in other galaxy parameters to compensate for these errors. This is also demonstrated in Table 1, where it is apparent that our models can accurately reproduce the colours of galaxies with ongoing star formation. This situation is unlikely to hold in the UV, however, as prescriptions for the dust extinction law start to diverge at these short wavelengths (Calzetti, Kinney, & Storchi-Bergmann 1994).

Both the UV-upturn and the uncertain effects of dust reddening in the far-UV lead us to place little confidence in our model UV colours. We should therefore avoid this spectral region if possible.

In addition, it should be noted that we neglect emission from star forming galaxies, such as the commonly observed [OII], [OIII] and Balmer features at locally (Kennicutt 1992) and at high redshifts (Hammer et al. 1997). This should not present a major problem, as the effects of line emission on broad band photometry is not large: A line width with an equivalent width of 20 Å in emission would cause only ~ 0.02 mag of brightening in the broad band magnitude.

Finally, we note that although most of redshift range below 1.5 can be covered by the standard Johnson-Cousins system including Z band, there are some particular redshift range where we have larger errors in the estimated redshifts; ie. $z < 0.25$, $0.4 < z < 0.5$, and $0.8 < z < 0.9$. At these redshift ranges, the effect of changing redshift on colours is hard to be distinguished from that of changing stellar population (Fig. 2). If we want to handle clusters in these redshift ranges with better precision, we need to use passbands in other pho-

tometric systems which properly bracket the 4000 Å break at the cluster redshifts.

3 BAYESIAN CLASSIFICATION

3.1 Basic scheme

A Bayesian approach allows us to incorporate our existing knowledge of galaxy populations, and thus to proportionally weight the areas of parameter space that we search. The Bayesian probability of a particular galaxy having a redshift z and bulge to total luminosity ratio B/T is given by the equation:

$$P_{\text{Gal}}(z, B/T) = P_1(z, B/T|m_B)P_2(z, B/T), \quad (5)$$

where $P_1(z, B/T|m_B)$ is the probability of a given galaxy of apparent magnitude m_B having a redshift z and bulge to total luminosity ratio B/T, and $P_2(z, B/T)$ is the probability of a given galaxy reproducing the observed galaxy colours. We first deal with the evaluation of $P_2(z, B/T)$, ie. the probability of a given model galaxy reproducing the observed galaxy colours.

The basic philosophical approach used for this redshift estimator is the comparison of a galaxy's location on a colour-colour plot and a finely-spaced grid of models superimposed on that plot to estimate the properties of that galaxy. The magnitudes of the observed galaxy are made into colours, and the errors in the colours used to make up a covariance matrix, describing the sizes of the colour errors, and their relationships. Then, for all of the model galaxy colours, the difference between them and the observed colours are calculated. Under the assumption that the photometric errors follow a Gaussian distribution, the probability that the model describes the galaxy colours adequately ($P_2(z, B/T)$) is given by:

$$P_2(z, B/T) = 1/[(2\pi)^n |\mathbf{C}|]^{1/2} \exp\{-1/2(\mathbf{u}^T \mathbf{C}^{-1} \mathbf{u})\}, \quad (6)$$

where n is the number of colours used, \mathbf{u} is the vector of differences between the model galaxy colours and the observed colours, \mathbf{C} is the covariance matrix of those colours, and $|\mathbf{C}|$ is the determinant of the covariance matrix. The diagonal elements of \mathbf{C} correspond to the variance in the individual colours. The off-diagonal elements correspond to the variance of any passbands in common between two colours, with the appropriate sign (which indicates whether the errors in a given passband affect the colours in the same or an opposite sense). Since we require galaxies to have small ($\lesssim 0.1$ mag) photometric errors in order to reliably determine their redshift, using a Gaussian rather than a log-normal is

Table 3. Adopted LF parameters.

Type	B/T	M_B^*	α	Φ^* ($\times 10^{-3}$ Mpc $^{-3}$)
E	1.0	-20.74	-0.85	0.188
S0	0.6	-20.25	-0.94	0.950
Sa-Sb	0.33	-20.23	-0.58	1.088
Sc-Im	0.0	-20.32	-1.07	0.625

an adequate representation of the error distribution in each band. This assumption considerably shortens the probability computation time. If it is impossible to find a satisfactory match to the galaxy colours, the galaxy is omitted from further consideration.

This procedure gives the probability that an observed galaxy is adequately described by a given model galaxy. This product is evaluated for a large number of plausible model galaxies with a range of B/T ratio and redshift. The other effects, such as age and metallicity of model galaxies are considered later in § 3.3. These evaluations makes up a ‘probability map’ on the plane of B/T ratio and redshift. In order for us to obtain the final probability, $P_{\text{Gal}}(z, \text{B/T})$ of the galaxy having a particular z and B/T, it is necessary to make up a prior distribution, given what is already known about galaxy populations.

3.2 Prior distribution

The quantity $P_1(z, \text{B/T}|m_B)$ is our prior distribution. The effect of the prior is to modulate the redshift estimates provided by the colour analysis by using magnitude information. Note that it makes little difference to the redshift estimate (well within the error bars of the redshift determination) *unless* there is a degeneracy, and the colour of two or more models satisfy the observational constraints equally well at different redshifts. In that case, it is designed to discover which one of these options is more likely to be observed, and weights the ‘probability map’ accordingly.

In forming the prior distribution, we need to know the type dependent luminosity function (LF) $\Phi(m_B, \text{B/T})$ and the volume element $dV/dz d\Omega$. Using these two elements, the prior is given as follows:

$$P_1(z, \text{B/T}|m_B) = dV/dz d\Omega \Phi(m_B, z, \text{B/T}). \quad (7)$$

These two parts are treated separately below.

3.2.1 The local luminosity function

In order to get $\Phi(m_B, \text{B/T})$ we use the local, type-dependent luminosity function (LF). However, there remains considerable uncertainty in the type-dependent LF, as the splitting into morphological types is carried out in a number of different ways, and the faint end slopes differ considerably between different studies (Marzke et al. 1998, Bromley et al. 1997, Marzke et al. 1994, Bingelli, Sandage, & Tammann 1988). We chose to adopt a variant of Marzke et al.’s (1994) determination in the Schechter (1976) form, which is parameterised by Φ^* , α and M_B^* . The parameters for the observed local luminosity function are summarised in Table 3 as a

function of the Hubble type. To connect between the Hubble types and B/T ratio, we use Simien & de Vaucouleurs (1986). The characteristic magnitude of the LF, $M_B^*(\text{B/T})$, corresponds to the apparent magnitude $m_B^*(z, \text{B/T})$ at a redshift z as:

$$m_B^*(z, \text{B/T}) = M_B^*(\text{B/T}) + DM(z) + \Delta M_B(z, \text{B/T}), \quad (8)$$

where DM is the distance modulus at redshift z in the adopted cosmology. ΔM_B is the absolute magnitude change in B -band in the observer’s frame due to the luminosity evolution and the shift of the wavelength shortwards with redshift, and is taken from the model. In this way, we finally obtain the LF in apparent magnitude m_B as a function of redshift and B/T ratio:

$$\Phi(m_B, z, \text{B/T}) = 0.92 \Phi^* e^{\{-0.92(\alpha+1)(m_B - m_B^*) - \exp(-0.92(m_B - m_B^*))\}}. \quad (9)$$

If the observed galaxy lacks B -band data, we use a prior in the band nearest to B . In this case, we make up the local LFs in the alternative band by shifting the B -band LFs using model colours of each type.

3.2.2 Volume element

The other essential ingredient of the prior is the volume element $dV/dz d\Omega$. The formula for the volume element as a function of redshift was taken from Carroll, Press, & Turner (1992), with the addition of some factors of c to satisfy dimensionality considerations, and allows variations in Ω_0 , H_0 and the inclusion of the cosmological constant via the term Λ_0 :

$$dV/dz d\Omega = \frac{d_M^2}{\{1 + \Omega_k (H_0 d_M/c)^2\}^{1/2}} \frac{d(d_M)}{dz}, \quad (10)$$

where, Ω_k is given by $\Omega_k = -\frac{kc^2}{R_0^2 H_0^2}$, and R_0 is the scale factor of the universe and k is the curvature of the universe. The quantity d_M is the proper motion distance, and in this case is given by:

$$d_M(z) = \frac{c}{H_0 |\Omega_k|^{1/2}} \text{sinn}(|\Omega_k|^{1/2} \mathcal{F}), \quad (11)$$

where ‘sinn’ is a function that equals sinh in an open universe, sin in a closed universe, and disappears in a critical universe, and \mathcal{F} is given by:

$$\mathcal{F} = \int_0^z [(1+z')^2(1+\Omega_0 z') - z'(2+z')\Lambda_0]^{-1/2} dz', \quad (12)$$

which must be integrated numerically for most non-trivial cosmologies.

3.2.3 Comparison with observation

The prior was used to calculate the $n(z)$ distribution within a magnitude range $22.5 < m_B < 24.0$. This calculated distribution was then compared to the observed redshift distribution of galaxies within the same magnitude range given by Glazebrook et al. (1995) and Cowie et al. (1996). The comparison is shown in Fig. 4. It is clear that the prior reproduces the overall form of the observed $n(z)$ diagram.

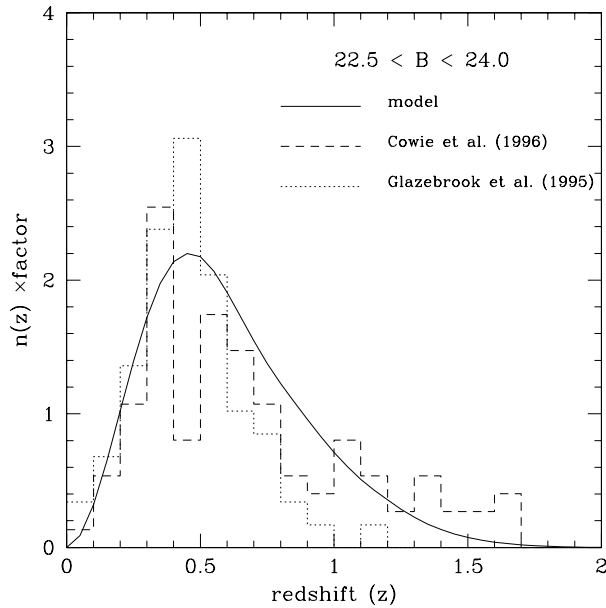


Figure 4. The observed $n(z)$ distributions for a sample of galaxies in the magnitude range $22.5 < m_B < 24.0$ from Glazebrook et al. (1995) and Cowie et al. (1996) are plotted against the expectation for the $n(z)$ distribution calculated from our prior distribution. The overall shape is in adequate agreement with the observational data.

3.2.4 The effect of the prior

It should be noted that the prior distribution is quite model-dependent, because the type-dependent local LF is ill-constrained, and because the detailed type-dependent spectral evolution is poorly understood. Also, here we make two assumptions: ie., that there is no number evolution of galaxies, and that there is no size dependent luminosity evolution, that is that galaxies with similar B/T ratios have the same colours at all redshifts, regardless of their total luminosity. These assumptions and ingredients may be inadequate to describe the real universe, especially in the context of a hierarchical clustering universe. However, these uncertainties are not so important, because the estimated redshift is essentially determined by the colour term (P_2 in Eq. 5), and the prior (P_1) is used supplementarily. The prior becomes important when the solution from the colour term splits into multiple redshift ranges. In such a case, the prior works to avoid unreasonable solutions of redshift for a given apparent magnitude. This situation is illustrated in Fig. 5. The figure shows an example of the probability maps of a given galaxy. The colour term gives two solutions, one at low redshift ($z \sim 0.2$) and the other at high redshift ($z \sim 1.0$), but the prior rejects the solution with higher redshift based on the brightness of the galaxy.

We also tested the effect of local LF on the final estimated redshift through the prior by changing the LF parameters listed in Table 3. We shifted M_B^* by ± 0.5 magnitude for all types, resulting in a shift of the redshift peak of the $n(z)$ distribution in Fig. 4 by ∓ 0.1 , and we tried fixing the faint end slope α at -1 for all types. In all cases, however, the change in the final estimated redshifts was well

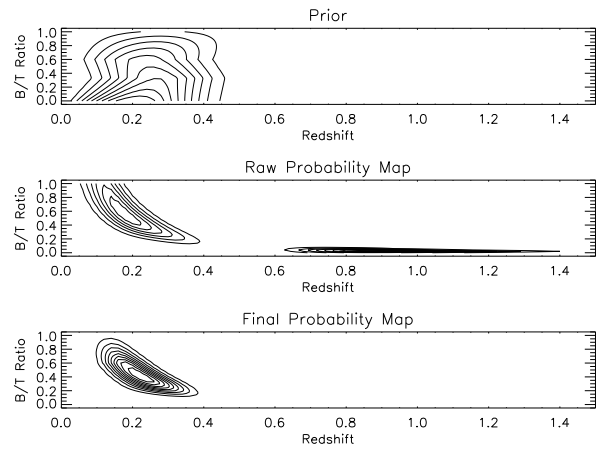


Figure 5. Probability maps for a given galaxy with $m_V = 20.3$. The contours indicate linear probabilities in steps of 0.1 from the maximum. Top panel shows the prior distribution (P_1), while the middle panel indicates the probability map from the colour information only (P_2). The bottom one is the final combined probability map. The prior rejects the high redshift solution (which is permitted, when considering only the galaxy’s colours) based on the brightness of the galaxy.

within the estimated redshift errors. This experiment shows our method is robust to uncertainties in the prior estimation.

3.3 The models included in the classifier

The estimates of redshift and galaxy type will depend quite sensitively on the detailed choice of model galaxy template. In § 2.2, we investigated the various effects on the galaxy colours, namely the effects of age, metallicity, disk light addition, recent star bursts, reddening, and cosmology. However, many of these effects were found to be degenerate with one another. In these models, effects due to age, metallicity, reddening and changes in cosmology are particularly degenerate. Therefore, by including only the metallicity effect explicitly in the classifier, we also cover the other three effects at the same time as they behave just like metallicity variations. To this aim, we considered four B/T sequences with different bulge metallicities. Each sequence gives different probability map on the redshift and B/T plane, and then they are combined into a single ‘probability map’ by performing a mean of the separate maps. This mean is in essence a weighted mean, as the most plausible metallicity for the model galaxies will have the best match to the colours. In this way, we take into account the metallicity effects explicitly, and hence the other degenerate effects.

The remaining significant effect which is not covered is that of a recent burst of star formation. As seen in Fig. 2 large amounts of relatively recent star formation can make a galaxy look as if it has a lower redshift than it actually does, if the colours are interpreted as being entirely due to redshift, B/T and metallicity effects. They might be simply assigned significantly underestimated redshifts. However, as already shown, unless burst strength f_b is as high as $> 15\%$ and the burst age $T_b \sim 0.5$ Gyr, the burst population colour change is similar to those resulting from other effects. These

populations should be short lived and are expected to be rare. Therefore omitting the recent star burst model will not affect our global redshift estimation. We should note, however, this could be a problem if significant fraction of cluster members would be strongly affected by a recent burst, due to cluster-cluster merging for example. In such a case, we would need to include the extra set of models of recent star burst to correctly estimate redshifts, although it would lead to greater estimation errors.

3.4 Error estimates

At this stage, the redshift and galaxy type estimates are in the form of the ‘probability map’ $P_{\text{Gal}}(z, B/T)$. However, an estimate of a given galaxy’s redshift and type is often required for eg. comparison with real redshifts, or cluster member identification. Best estimates for redshift ($z_{\text{estimated}}^{\text{best}}$) and effective 1σ confidence intervals ($z_{\text{estimated}}^{\text{min}}$, $z_{\text{estimated}}^{\text{max}}$) are obtained by taking the $P_{\text{Cum}}(z) = 0.5$ and the $P_{\text{Cum}}(z) = [0.16, 0.84]$ intervals, respectively, of the cumulative distribution:

$$P_{\text{Cum}}(z) = \int_0^z dz' \int_{B/T=0}^{B/T=1} d(B/T) P_{\text{Gal}}(z', B/T). \quad (13)$$

These error estimates depend on the estimated photometric errors: through the use of the covariance matrix \mathbf{C} , the error estimates in the photometry are explicitly included in the determination of $P_2(z, B/T)$. Large uncertainty in the colours propagates through into larger uncertainties in the $(z, B/T)$ combinations capable of adequately reproducing the observed colours. It is important to know how much photometric accuracy we need to achieve the error in redshift within the expected bound, as it will certainly constrain the accuracy of any future applications of this method.

To produce redshift error estimates as a function of photometric accuracy, simulations using 100 galaxies with $K < 20$, chosen at random in the range of $0 < B/T < 1$ and $0.2 \leq z \leq 1.8$ were undertaken. The bulge metallicity $\langle [M/H] \rangle_{\text{bulge}}$ was chosen randomly between 0.061 and -0.523 . After allocating the model magnitude in each passband for each galaxy, Gaussian photometric errors were then applied. We used these magnitudes and photometric errors of the simulated galaxies in the course of the redshift estimation. Here *BVRIK* passbands were used. The quantities $\sigma(\Delta z)$ and $\sigma(\text{error})$, corresponding to the root mean square (RMS) of real and estimated redshift error respectively, were then plotted in Fig. 6 where:

$$\Delta z = z_{\text{estimated}}^{\text{best}} - z_{\text{real}}, \quad (14)$$

$$\text{error} = (z_{\text{estimated}}^{\text{max}} - z_{\text{estimated}}^{\text{min}})/2, \quad (15)$$

$$\sigma(\Delta z) = \sqrt{(\Delta z)^2}, \quad (16)$$

$$\sigma(\text{error}) = \sqrt{\text{error}^2}. \quad (17)$$

As seen from the solid lines, both $\sigma(\Delta z)$ and $\sigma(\text{error})$ increase with photometric error. Importantly, even the photometric error is as bad as 0.15 magnitudes in all bands, the average redshift error $\sigma(\Delta z)$ is still kept smaller than 0.1. As for the estimated redshift error $\sigma(\text{error})$, it is roughly comparable to the photometric error.

Table 4. Passband choice for random galaxy simulations.

passbands	all		E/S0	
	$\sigma(\Delta z)$	$\sigma(\text{error})$	$\sigma(\Delta z)$	$\sigma(\text{error})$
<i>BVRIK</i>	0.065	0.076	0.060	0.074
<i>RIK</i>	0.127	0.135	0.121	0.129
<i>BVRI</i>	0.178	0.199	0.176	0.210

Next we consider the effect of mis-estimation of the photometric error on the redshift estimation error. It is possible that if the errors are under- or over-estimated, the redshift estimator will make the distribution of likely $(z, B/T)$ too broad or multiply-peaked, reducing the accuracy of the redshift estimate. Therefore, it is important to test the effects that uncertainty in the determination of the errors can have on the redshift estimate accuracy. We realise this situation by fixing the real photometric error at 0.071 mag and varying the estimated photometric error going into the covariance matrix \mathbf{C} . The result is shown by the dashed lines in Fig. 6. It is clear that the under- or over-estimation of the photometric errors has little, if any, effect on the quality of redshift estimation $\sigma(\Delta z)$. Errors in the determination of the photometric quality, do however have a marked effect on the *estimated* quality of the redshift determination, given by $\sigma(\text{error})$. It is clear, therefore that it is important to be careful in the estimation of the photometric errors in order to estimate the quality of the redshift determination effectively.

The quality of the redshift estimation also sensitively depends on the passband choice. We investigated three sets of passbands for the randomly generated galaxies with 0.071 mag photometric errors, and the results are summarised in Table 4. With *RIK* passbands, the result is about factor of two worse than the *BVRIK* case. This is because it gets harder to disentangle the colour degeneracies between lower redshift early-types and higher redshift late-types without using bluer colours *B* and *V*. If, instead, we do not use *K*-band colours, the quality of the redshift estimation worsens, as high redshift galaxies with $z > 0.8 - 1.0$ no longer have a passband longwards of the 4000 Å break. It is therefore important to choose the passbands carefully for photometric redshift estimation according to redshift ranges under consideration and the depth of the photometric sample.

4 TESTING

In this section, we focus on testing our method using photometry for galaxies with known spectroscopic redshifts. Because we wish to focus on the recovery of high redshift clusters at $z \gtrsim 1.0$, it would be best to test with an extensive dataset for a real high redshift cluster. However, such data is not available at the moment, since we need both multi colour photometry covering the 4000 Å break (at least 3–4 bands) and spectroscopically determined redshifts for individual galaxies. Therefore, we have decided to test our method with two independent sets of data: a well-studied cluster Abell 370 at $z = 0.374$, and the Hubble Deep Field.

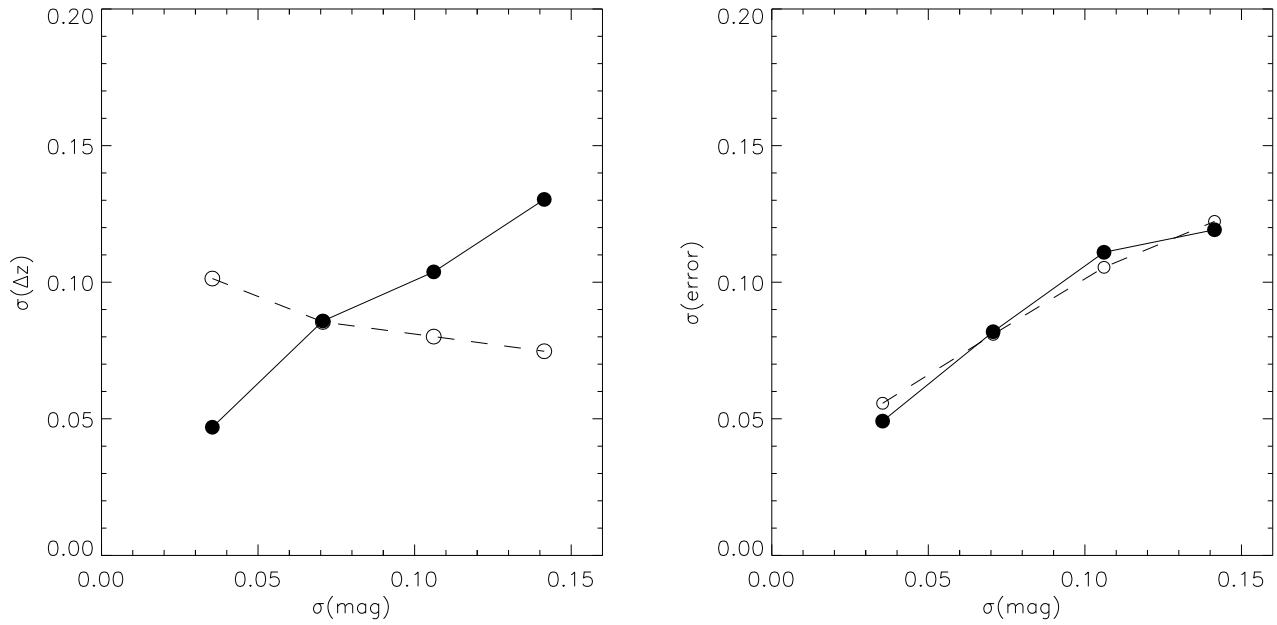


Figure 6. The effects of photometric error on the quality of redshift estimation. Simulations with 100 galaxies using the B , V , R , I and K passbands were used to assess the effects of changing photometric quality in magnitude in all bands (solid lines). The RMS difference between the best estimate and the real redshift ($\sigma(\Delta z)$) is plotted against the Gaussian photometric error ($\sigma(\text{mag})$) in the left panel, while the RMS redshift error ($\sigma(\text{error})$) is plotted in the right panel. The effects of under- or over-estimation of the photometric error were also assessed by keeping the real photometric error fixed at 0.071 mag, and varying the estimated photometric errors going into the covariance matrix \mathbf{C} (dashed lines).

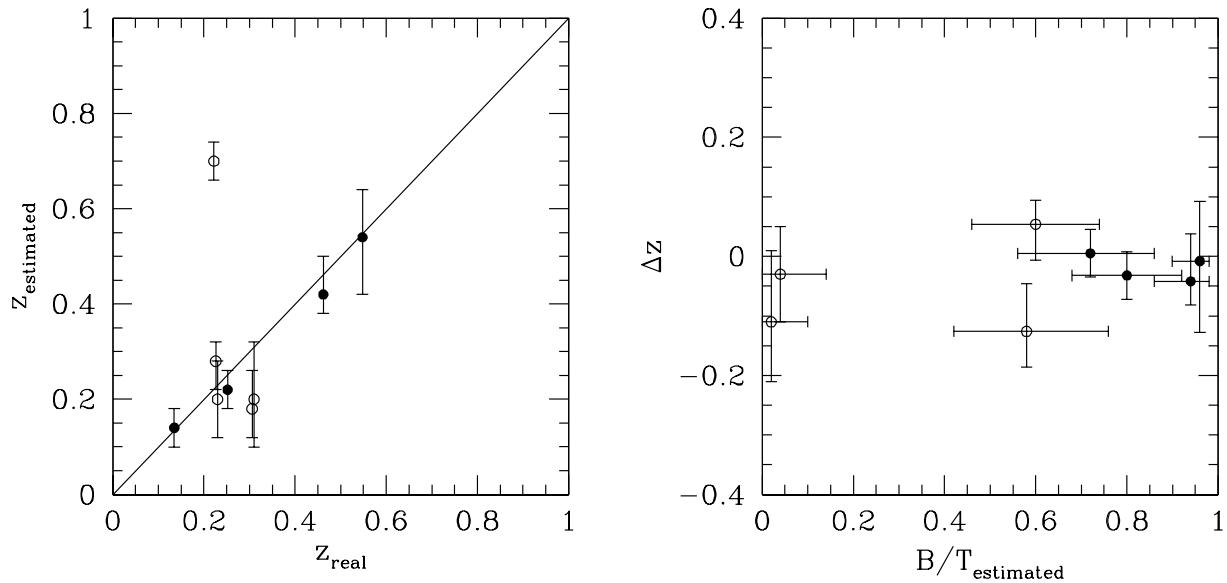


Figure 7. Field galaxies in the Abell 370 cluster field. Estimated redshift vs. spectroscopically determined redshift (left), and redshift error vs. estimated B/T ratio (right). Filled circles indicate E/S0 galaxies, while open circles indicate disk galaxies and those without morphological information.

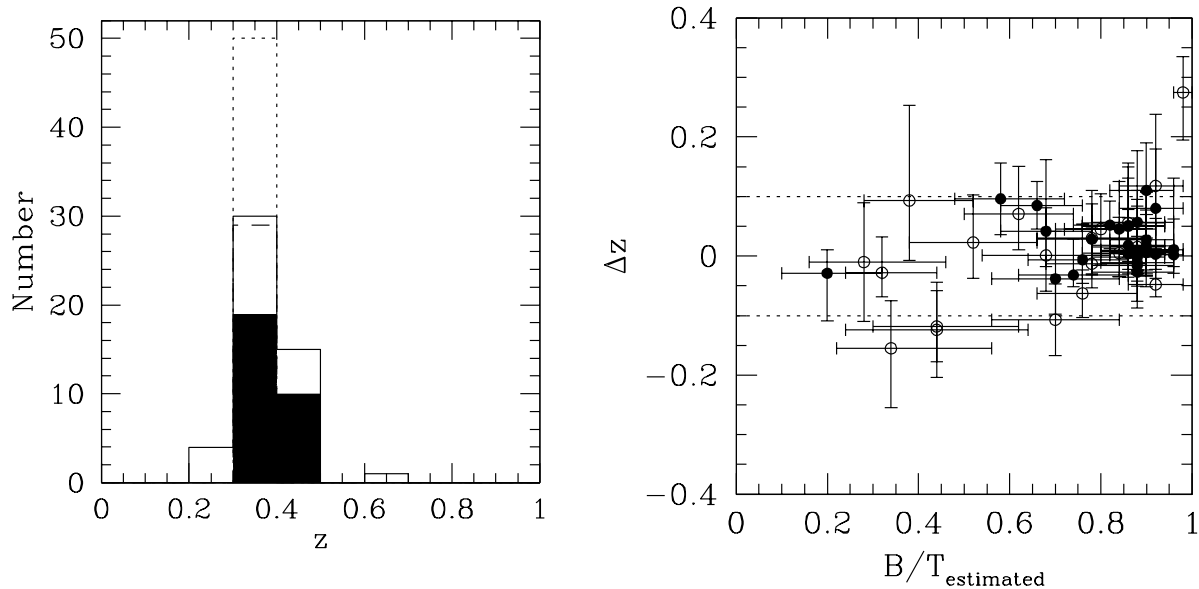


Figure 8. Cluster members of Abell 370. Distribution of the estimated redshifts (left) and redshift error vs. estimated B/T ratio (right). The filled histogram and filled circles indicate E/S0 galaxies, while the open histogram and open circles indicate disk galaxies and those without morphological information. The dotted and dashed histograms show the real redshifts of all types and E/S0's, respectively. The two dotted lines (right) show the region of $|\Delta z| < 0.1$ where galaxies are taken to be cluster members.

4.1 Abell 370

The photometric data are taken from Pickles & van der Kruit (1991). We use their *BVRI* photometry, using a 7 arcsec aperture. For our use, we selected 59 galaxies which have spectroscopically determined redshifts. The redshifts are mainly taken from Pickles & van der Kruit (1991) and supplementarily from Stanford, Eisenhardt, & Dickinson (1995), although the latter gives only cluster memberships to which we assigned the cluster mean redshift $z = 0.374$. To separate the sample of E/S0 galaxies, we use galaxy morphology as given by HST images (Stanford et al. 1995). As Abell 370 has a redshift $z = 0.374$, the filter combination (*BVRI*) is expected to work to pick out cluster members to some extent as they bracket the 4000 Å break (§ 2.2), although *U*-band is missing which is important to discriminate galaxies with lower B/T ratios at the cluster redshift from those with higher B/T ratio at lower redshifts. However, unfortunately, the photometric accuracy is poor, especially in *B* and *I* bands (0.13–0.19 mag in *B*, 0.04–0.08 mag in *V*, 0.03–0.07 mag in *R* and 0.08–0.16 in *I*).

We estimated the photometric redshifts for our sample galaxies. The results for field galaxies and cluster members are shown separately in Figs. 7 and 8, respectively. The cluster members are defined as those which have spectroscopic redshifts $0.374 - 0.02 < z < 0.374 + 0.02$. As for the E/S0 galaxies, we can estimate the redshifts very well within $|\Delta z| < 0.1$ both for field galaxies and cluster members. On the other hand, some disk galaxies have over- or under-estimated redshifts. In Fig. 7, there is a galaxy with $\Delta z > 0.4$. That is because the photometry in *I*-band of this galaxy is very poor as indicated in the original table in Pick-

les & van der Kruit (1991), and in fact if we use only *BVR* bands for this galaxy, the estimated redshift agrees with the real redshift at the 1.5σ level. The other two field disk galaxies are slightly underestimated by $\Delta z \sim -0.1$. These galaxies have very blue colours in *B - V* or *V - R*, and it is suggested that they are either disk dominated galaxies or the ones strongly influenced by a recent star burst. For the cluster members (Fig. 8) also, there are some galaxies whose redshifts are underestimated as much as $\Delta z \sim -0.15$. These galaxies tend to have low estimated B/T ratios and are again degenerate with galaxies at lower redshift. The discrimination between a blue cluster member and a slightly redder galaxy at lower redshift can be difficult, especially when we lack a bluer band corresponding to far-UV region (2500-3000 Å).

Nevertheless, if we adopt the criteria of defining cluster members as $|\Delta z| < 0.1$, we can pick out most of the cluster members with little field contamination as shown in Figs. 9 and 10. This is especially true for early-type galaxies. As a result, the *C-M* relation of the E/S0 galaxies is well recovered (Fig. 9). The solid line shows the real relation for the real cluster members while the dashed line shows the estimated relation for the estimated cluster members. We used a bi-weight fitting method to calculate these *C-M* relations (Beers, Flynn, & Gebhardt 1990). Both relations are nearly identical.

In summary, although the photometric accuracy is not ideal, we can still pick out most of the cluster members in A370, especially early-type galaxies, only photometrically based on our method. The field contamination is negligibly small. The method has difficulty in recovering cluster mem-

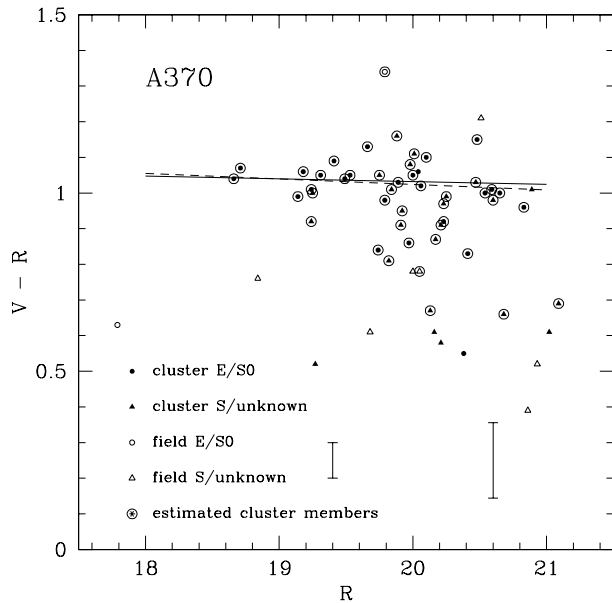


Figure 9. The C - M diagram for Abell 370. The filled symbols indicate cluster members, while the open symbols show field galaxies. The symbols surrounded by a large circle indicate the estimated cluster members selected using $|\Delta z| < 0.1$. Two error bars at the lower part of the figure indicate the typical one sigma observational errors. The solid and dashed lines indicate the C - M relation of the the real cluster E/S0's and that of the estimated cluster E/S0's, respectively, calculated using bi-weight fitting to the data.

bers bluer than $V - R = 0.6$, but this would be improved if U -band data were available.

4.2 Hubble Deep Field

To further test our method, we apply it to galaxies taken from the Hubble Deep Field. The galaxies used here are chosen from Cowie's K -selected galaxy sample (<http://www.ifa.hawaii.edu/~cowie/k.table.html>), all of which have spectroscopic redshifts, mainly from Cohen et al. (1996). Isophotal magnitudes in four HST WFPC2 filters (F300W[U_{300}], F450W[B_{450}], F606W[V_{606}], and F814W[I_{814}]) are taken from Williams et al. (1996). We cross-identify galaxies between Cowie's catalogue and the photometry catalogue using RA and DEC. We choose only isolated galaxies to avoid mis-identification. Also we excluded galaxies with $z > 2$, as the current passbands no longer bracket the 4000 Å break. Photometric errors are calculated from S/N ratios, but for those less than 0.05 magnitude, we assume a minimum error of 0.05 magnitude. We give larger minimum error of 0.2 magnitude to U_{300} for galaxies with $z_{\text{estimated}}^{\text{best}} > 0.2$, and to B_{450} for galaxies with $z_{\text{estimated}}^{\text{best}} > 0.8$, in order to avoid incorporating uncertain model far-UV colours. This is an iterative approach, but is unavoidable given the uncertainty of the model UV spectrum. The infrared photometry data in J are acquired from Cowie's table. A photometric accuracy of 0.1 magnitude is assumed in J -band as no information is given.

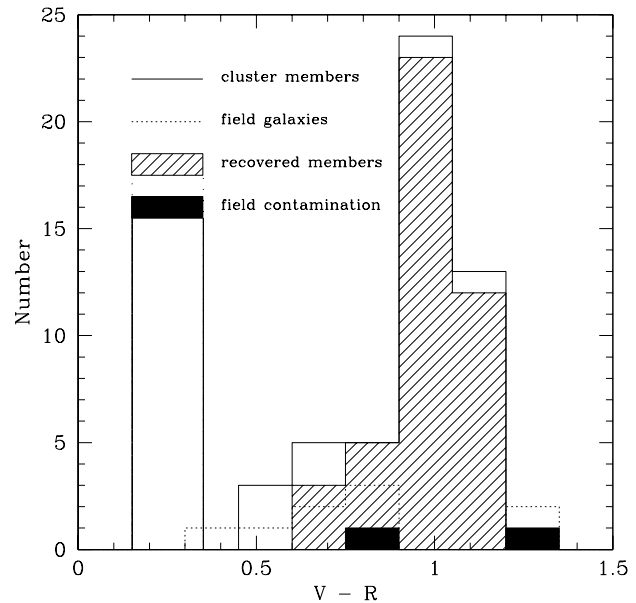


Figure 10. The colour histogram for Abell 370. The solid line shows the real cluster members, and the dotted line shows the real field galaxies. The slantwise hatched area indicates recovered cluster members, while the black shaded area indicates field contamination. It is shown that most of the cluster members are recovered, although a small number of the bluest galaxies are dropped out. This would be improved if the U -band data were available. Field contamination is also negligibly small.

Applying the model directly to this data set, we find a systematic offset of $\Delta z \sim -0.1$ between the real redshifts and the estimated redshifts. The most likely cause of this discrepancy is a zero-point mismatch of order 0.1 magnitude between the data and the model in such a way that the model is slightly redder in optical colours and a bit bluer in far-UV colour. It might be the intrinsic zero-point uncertainty in the model, since it is comparable to the limitation of the current population synthesis models (Charlot, Worthey, & Bressan, 1996), although it is puzzling that a similar problem is not seen in Abell 370. To correct this situation, we shift the model zero-points for this case only: ie. +0.1 magnitude is added onto the model U_{300} , I_{814} , and J . With this zero-point shift, most of the redshifts of HDF galaxies are correctly estimated as shown in Fig 11. The RMS errors of the estimated redshift are smaller than 0.1; ie. $\sigma(\Delta z) = 0.091$ and $\sigma(\text{error}) = 0.075$. Although the zero-point mismatch is a problem, it is encouraging that our method can estimate redshifts correctly over a wide range of redshifts. However this exercise makes it clear that the model should be calibrated with real data rather than being applied blind to high redshift systems. This can be achieved using a handful of spectroscopically confirmed members of the target cluster without compromising the overall aim of examining the star formation histories of the galaxy populations.

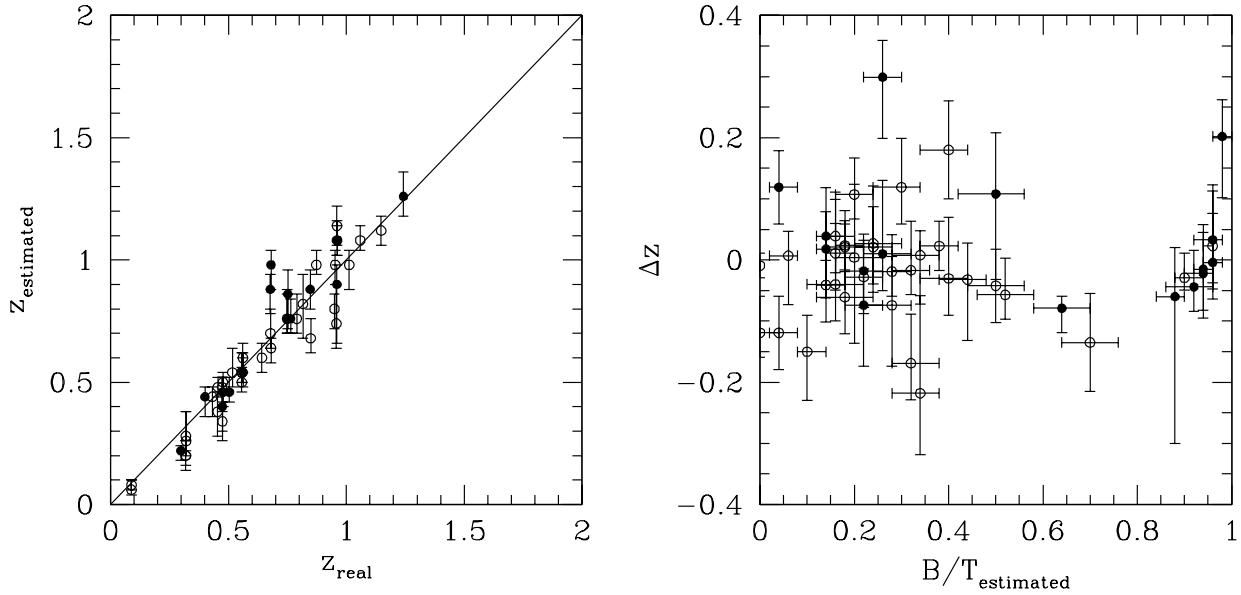


Figure 11. HDF galaxies. $U300, B450, V606, I814,$ and J passbands are used. Filled symbols indicate morphologically classified E/S0 galaxies, while the rest show other type galaxies or unclassified galaxies.

Table 5. Simulated galaxies in a $z = 1$ cluster field.

	type	n	$\langle [M/H] \rangle_{\text{bulge}}$	z_f	B/T
cluster	E/S0	10	$0.06 \sim -0.52$	4.5	1.0
		10	$0.06 \sim -0.52$	$4.5 \sim 1.5$	1.0
		10	$0.06 \sim -0.52$	4.5	$1.0 \sim 0.5$
	Sp	20	$0.06 \sim -0.52$	4.5	$0.5 \sim 0.0$
field	E	6	$0.06 \sim -0.52$	4.5	$1.0 \sim 0.6$
	S0	26	$0.06 \sim -0.52$	4.5	$0.6 \sim 0.5$
	Sab	17	$0.06 \sim -0.52$	4.5	$0.5 \sim 0.15$
	Sc-Im	5	$0.06 \sim -0.52$	4.5	$0.15 \sim 0.05$

5 APPLICATION TO HIGH REDSHIFT CLUSTERS

We are interested in applying this classifier to high redshift clusters around $z \gtrsim 1.0$, but, at present, a suitable data set is not available. To show the applicability of the classifier to targets at that redshift, we simulated a $z = 1$ cluster field using the model described in § 2. Although this is a self-consistency check (most importantly, it assumes that the photometric properties of real galaxies are accurately described by the stellar population synthesis code) it allows us to estimate the biases present in the recovered galaxies samples and to determine how much photometric accuracy and which combination of passbands is required to pick out cluster members effectively in such a cluster.

We generated field galaxies using the type dependent prior distribution outlined in § 3.2. The metallicity of the bulge was chosen so that $M_V^{\text{bulge}} = -23, -20$ and -17 measured at $z = 0$ corresponding to $\langle [M/H] \rangle_{\text{bulge}} = 0.06, -0.23,$

and -0.52 . Here we have simulated a K -limited galaxy sample with $m_K < 20$ for 1 arcmin² field of view which corresponds to 0.5 Mpc \times 0.5 Mpc at $z = 1$, using the prior distribution, taking the type-dependent LF into account. The number of galaxies in each type is summarised in the lower half of Table 5. As for the cluster members, we assumed the mix of galaxy populations given in upper half of Table 5; ie. 10 E/S0's from a metallicity sequence, another 10 E/S0's from an age sequence, and the other 10 E/S0's from a B/T sequence, and finally 20 disk galaxies are added in. Firstly, by using K -band luminosity functions of high redshift cluster galaxies (mean redshift 0.43) which are given separately for E/S0's and Spirals (Barger et al. 1998), we assigned K -band absolute magnitude at $z = 0.43$ for a given galaxy. Secondly, a formation epoch (z_f) and a B/T ratio are randomly assigned in the respective range given in Table 5. Then we can assign its bulge metallicity using its M_V^{bulge} at $z = 0$ calculated from M_K at $z = 0.43$. If a galaxy has $m_K > 20$ at $z = 1$, it is rejected from our sample, and the

Table 6. The bi-weight scatters and slopes of the C - M relation. The values for all types and E/S0 galaxies are shown separately. The scatters are measured with respect to the C - M relation of E/S0 galaxies only.

		Abell 370		$z = 1$ cluster	
		all	E/S0	all	E/S0
scatter	real	0.125	0.073	0.613	0.169
	estimated	0.112	0.072	0.603	0.189
slope	real	-0.018	-0.008	-0.423	-0.165
	estimated	-0.018	-0.016	-0.381	-0.165

process is repeated until we finally obtain 50 cluster galaxies in total. We assigned the model magnitudes in various bands for each galaxy both in the field and in the cluster. A Gaussian photometric error with $\sigma = 0.071$ is added on each colour of each galaxy. We then regard these generated photometric data as the observational ones for the $z = 1$ cluster field, and the redshift classifier is applied to each galaxy to estimate a redshift.

5.1 Biases in the recovered galaxy properties

The results for the field galaxies and the cluster members are shown separately in Figs. 12 and 13. We used $VRIC$ colours to estimate the redshifts. B -band was not used, since at $z = 1$ it falls in the far-UV spectral region, well below 2500 Å. The overall agreement between the estimated redshift and the real redshift is excellent. Most of the galaxy redshifts are well recovered within $|\Delta z| = 0.1$, regardless of real redshift and irrespective of galaxy type. As a result, as shown in Fig. 14, the recovery of cluster members is magnificent. Here we adopted the criterion of cluster members as $|\Delta z| < 0.1$, considering the photometric accuracy (see Fig. 6). It is also adequate since it does not pick up large amount of field contamination at high redshifts. In this case, only one cluster spiral is dropped out. Field contamination is also negligible (only four galaxies). We have recovered not only old ellipticals, but also young or star forming ellipticals and spirals as well. To see the bias in the identification of cluster members as a function of galaxy colour, we show the colour histogram of the recovered cluster members and the field contamination in Fig. 15. As is clear from the figure, there is no colour bias at all in either the cluster or the field. Consequently, we recover the C - M relation of E/S0 galaxies very well (identically in this case), as shown by the solid line in the figure. The bi-weight scatters around the relation are also calculated and given in Table 6 as well as the values of the C - M slope. The numbers for Abell 370 are also given in the same table. Both scatters and slopes are almost correctly estimated irrespective of galaxy type.

All the above results are encouraging. If the models were perfect, we could assign redshift with 0.1 accuracy or better with < 0.1 mag photometric errors in all bands. With this success, we will be able to extend the C - M relation analysis (eg., Kodama et al. 1998; Ellis et al. 1997; Stanford, Eisenhardt, & Dickinson 1998) to $z \gtrsim 1$ clusters without taking spectroscopic redshifts. Importantly, we can pick out cluster galaxies with various stellar populations; ie. not only passively evolving old galaxies but also the galaxies which have

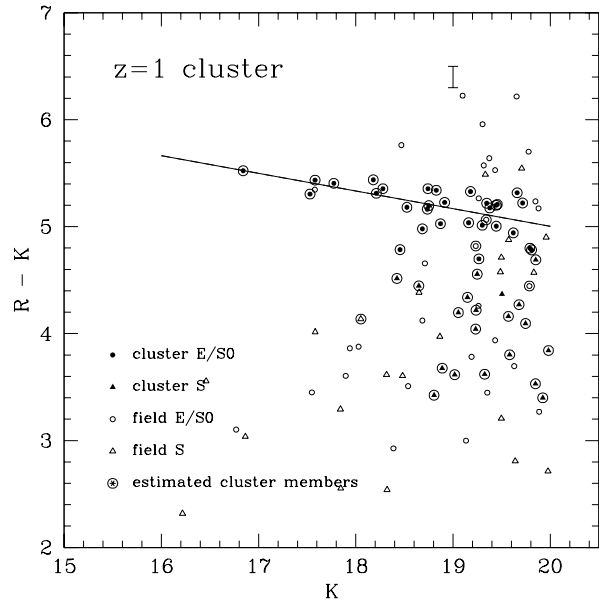


Figure 14. The C - M diagram for a simulated cluster field at $z = 1$. Caption is the same as Fig. 9. Note that the real C - M relation and the estimated one are identical (solid line).

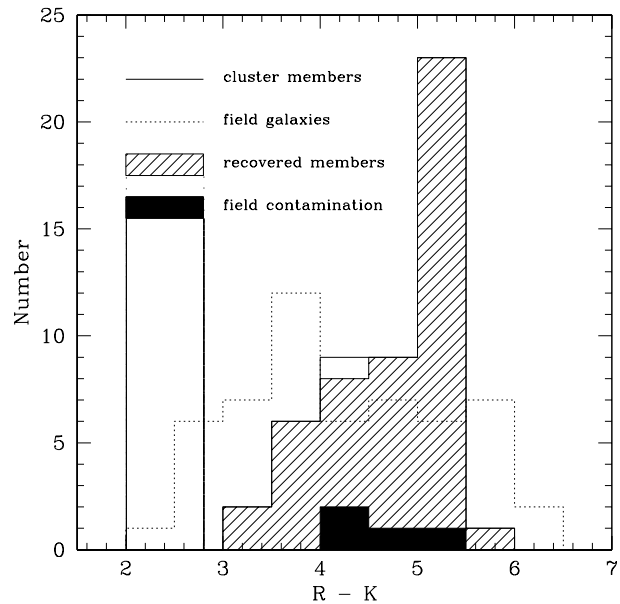


Figure 15. The colour histogram of a simulated cluster field at $z = 1$. The solid line shows the real cluster members, and the dotted line shows the real field galaxies. The slantwise hatched area indicates recovered cluster members, while the black shaded area indicates field contamination. There are few dropped out members and little field contamination, and importantly they have no bias in colours.

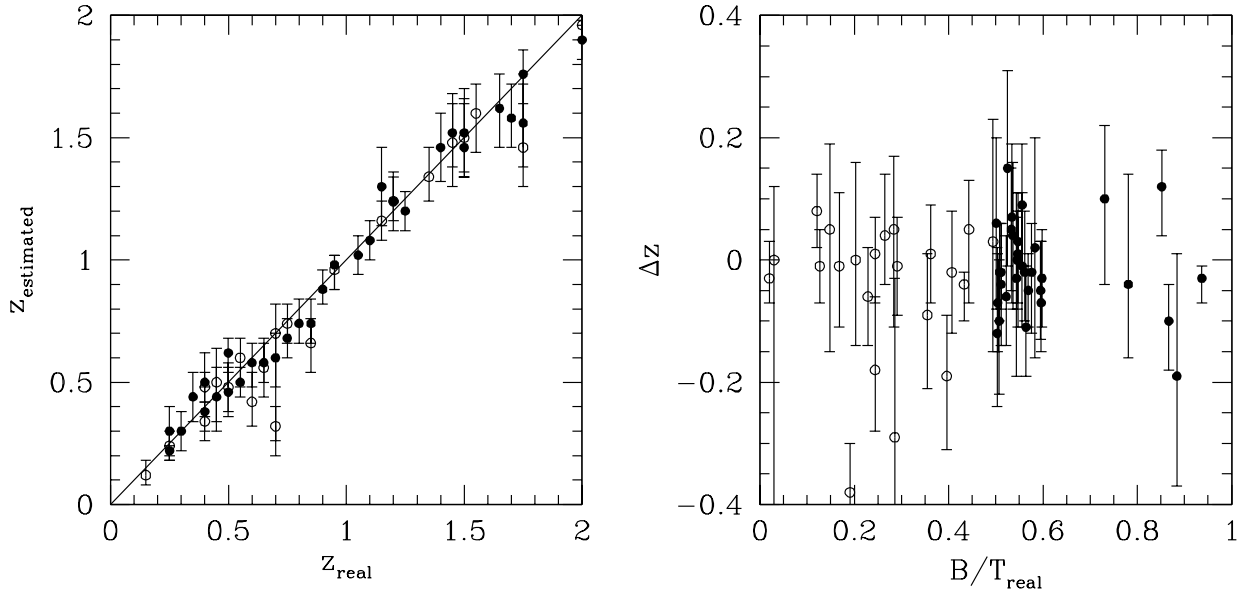


Figure 12. Field galaxies in the simulated cluster field at $z = 1$. Plotted are the estimated redshift vs. input real redshift (left), and redshift error vs. input real B/T ratio (right). Redshifts are estimated using *VRIK* passbands with random Gaussian photometric errors of $\sigma = 0.071$ magnitude in all bands. Filled circles indicate E/S0 galaxies defined as $B/T \geq 0.5$, while open circles indicate disk galaxies with $B/T < 0.5$.

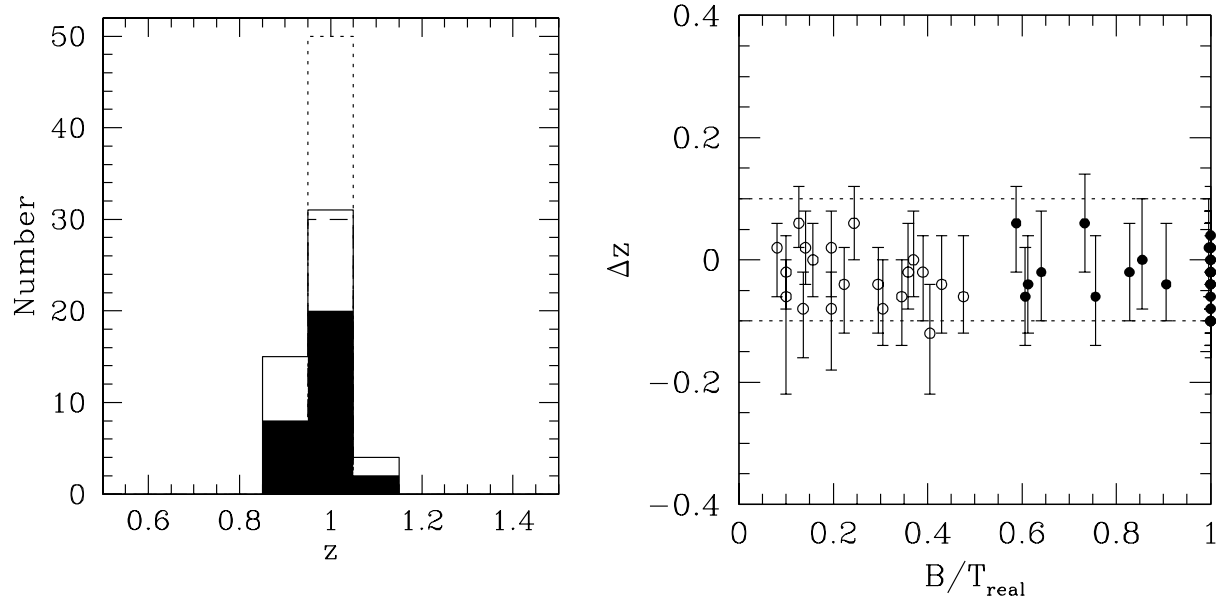


Figure 13. Cluster members in the simulated cluster field at $z = 1$. Distribution of the estimated redshifts (left) and redshift error vs. input real B/T ratio (right). Caption for the lines and the symbols are the same as Fig. 8.

a significant contribution from younger stellar populations. This is encouraging, as it is important to select the cluster members with as little bias as possible. Our method will allow us to conduct the colour scatter analysis around the $C-M$ relation reliably, and to look into the age dispersion of cluster galaxies at high redshifts, if any.

5.2 Optimal passbands for cluster identification

In Table 7, we summarise the effect of passband choice on the estimated redshift error. Photometric errors of 0.071 mag are assumed in all passbands. Two cases in particular are found to be ideal: $BVRIK$ and $VRIK$. The redshift errors are always well below 0.1 regardless of galaxy type, and hence the number of galaxies dropped out of our cluster sample, and the field contamination, are minimised. It is encouraging that we can do comparably well without B -band, as it is good to minimise the use of passbands shortwards of rest frame 2500 Å where possible. It should be noted that VIK and VRK work comparably well, although $\sigma(\text{error})$ is larger, especially for galaxies with ongoing star formation. This is because it becomes difficult to separate the effects of changes in stellar population and those of changing redshift. If both B and V -band are missing (and we have RIK only), we tend to underestimate the redshift of bluer galaxies. This is analogous to lacking U -band for Abell 370: it becomes difficult to disentangle galaxy type and redshift without the UV colours for star forming galaxies. For the early type galaxies, however, the redshift errors are reasonable, as we would expect from Fig. 2. In contrast, if K band is missing, the errors in the redshift estimation become much larger, irrespective of galaxy type, as there is no passband longwards of the rest-frame 4000 Å break. In this context, it is crucial for high redshift work to have both optical and near infrared passbands for accurate redshift estimation.

6 SUMMARY

We present a new photometric redshift estimator, which is optimised for the identification and study of galaxy clusters at high redshifts. We use only several broad passbands covering the 4000 Å break, and find in practice that it is possible to avoid the use of the uncertain colours shortwards of rest frame 2500 Å. In our models, we considered as wide a variety of stellar populations as is possible to minimise the selection bias in the recovered cluster members. As most of the effects of changing stellar population on the integrated colours are highly degenerate, we find that it is possible to estimate redshifts with reasonable accuracy for a range of galaxy types, ranging from those with old, passively evolving stellar populations, through to those with younger stellar populations and on-going star formation.

Following the success in testing our method with data from Abell 370 and from the Hubble Deep Field, we applied it to a simulated cluster at $z = 1$. We have shown that the estimation of redshifts with accuracies better than $|\Delta z| < 0.1$ can be achieved with multi-passband photometry of moderate quality (≈ 0.1 mag) in a small number of passbands, and the cluster members can be reliably identified. Therefore, the recovery of the $C-M$ relation both in terms of the slope and scatter is expected to be accurate and almost free

from any selection bias. We now have a means of analysing the *photometric* properties of cluster galaxies at very high redshifts without a thorough spectroscopic membership confirmation.

ACKNOWLEDGEMENTS

We would like to thank C. Tadhunter and S. Warren for useful discussion. We are also grateful to the anonymous referee who gave us many constructive comments. T.K. thanks JSPS Postdoctoral Fellowships for Research Abroad for financial support. E.F.B. would like to thank the Isle of Man Education Department for their generous financial support. This project made use of STARLINK computing facilities at Durham and Cambridge.

REFERENCES

- Allington-Smith, J., et al., 1994, *PASP*, 106, 983
Arimoto, N., 1996, in: *From Stars to Galaxies*, eds. C. Leitherer, U. Fritze-von Alvensleben, J. Huchra (ASP Conf. Ser. Vol. 98), p.287
Barger, A. J., Aragón-Salamanca, A., Smail, I., Ellis, R. S., Couch, W. J., Dressler, A., Oemler, A., & Poggianti, B. M., 1998, *ApJ*, in press
Baugh, C. M., Cole, S., Frenk, C. S., & Lacey, C. G., 1998, *ApJ*, in press
Beers, T. C., Flynn, K., & Gebhardt, K., 1990, *AJ*, 100, 32
Berlind, A. A., Quillen, A. C., Pogge, R. W., & Sellgren K., 1997, *AJ*, 114, 107
Bica, E., 1988, *A&A*, 195, 76
Binggelli, B., Sandage, A., & Tammann, G. A., 1988, *ARA&A*, 26, 509
Bower, R. G., Lucey, J. R., & Ellis, R. S., 1992a, *MNRAS*, 254, 589
Bower, R. G., Lucey, J. R., & Ellis, R. S., 1992b, *MNRAS*, 254, 601
Bower, R. G. & Smail, I., 1997, *MNRAS*, 290, 292
Bromley, B. C., Press, W. H., Lin, H., & Kirschner, R. P., 1997, *astro-ph/9711227*
Bruzual, G. A. & Charlot, S. 1993, *ApJ*, 405, 538
Burstein, D., Bertola, F., Buson, L. M., Faber, S. M., & Laner, T., 1988, *ApJ*, 328, 440
Buta, R., Mitra, S., de Vaucouleurs, G., & Corwin, Jr. H. G., 1994, *AJ*, 107, 118
Buta, R. & Williams, K. L., 1995, *AJ*, 109, 543
Calzetti, D., Kinney, A. L., & Storchi-Bergmann, T., 1994, *ApJ*, 429, 582
Carroll, S. M., Press, W. H., Turner, E. L., 1992, *ARA&A*, 30, 499
Charlot, S., Worthey, G., & Bressan, A., 1996, *ApJ*, 457, 625
Cohen, J. G., Cowie, L. L., Hogg, D. W., Songaila, A., Blandford, R., Hu, E. M., Shopbell, P., 1996, *ApJ*, 471, 5
Connolly, A. J., Csabai, I., Szalay, A. S., Koo, D. C., Kron, R. G., & Munn, J. A., 1995, *AJ*, 110, 2655
Cowie, L. L., Songaila, A., Hu, E. M., & Cohen, J. G., 1996, *AJ*, 112, 839
de Jong, R. S., 1996, *A&A*, 313, 377
de Vaucouleurs, G., de Vaucouleurs, A., Corwin, H. G., Buta, R. J., Paturel, G., & Fouqué, P., 1991, *Third Reference Catalog of Bright Galaxies* (Springer;Berlin) (RC3)
Deltorn, J.-M., Le Fevre, O., Crampton, D., & Dickinson, M., 1997, *ApJ*, 483, 21
Ellis, R. S., Smail, I., Dressler, A., Couch, W. C., Oemler Jr, A., Butcher, H., & Sharples, R. M., 1997, *ApJ*, 483, 582

Table 7. Passband choice for a simulated cluster field at $z = 1$. Numbers of dropped out members and field contamination are also presented. Percentage of dropped members and field contamination are defined per real cluster members and per estimated cluster members, respectively.

passbands	all		E/S0		dropped members		field contamination	
	$\sigma(\Delta z)$	$\sigma(error)$	$\sigma(\Delta z)$	$\sigma(error)$	all	E/S0	all	E/S0
<i>BVIK</i>	0.070	0.074	0.068	0.074	3 (6%)	3 (10%)	5 (10%)	4 (13%)
<i>VIK</i>	0.079	0.099	0.064	0.095	1 (2)	0 (0)	4 (8)	3 (9)
<i>VRK</i>	0.141	0.129	0.069	0.112	7 (14)	1 (3)	4 (9)	3 (9)
<i>VRI</i>	0.114	0.131	0.087	0.129	4 (8)	2 (7)	3 (6)	3 (10)
<i>RIK</i>	0.231	0.232	0.243	0.216	9 (18)	3 (10)	10 (20)	7 (21)
<i>RJK</i>	0.155	0.133	0.074	0.118	16 (32)	3 (10)	3 (8)	3 (10)
<i>RJK</i>	0.211	0.212	0.159	0.216	38 (76)	21 (70)	7 (37)	4 (31)

- Glazebrook, K., Ellis, R. S., Colles, M., Broadhurst, T., Allington-Smith, J. J., & Tanvir, N., 1995, MNRAS, 273, 157
- Gwyn, S. D. J. & Hartwick, F. D. A., 1996, ApJ, 468, L77
- Hammer, F., Flores, H., Lilly, S. J., Crampton, D., Le Fèvre, O., Rola, C., Mollen-Ornelas, G., Schade, D., & Tresse, L., 1997, ApJ, 481, 49
- Jablonska, P., Martin, P., & Arimoto, N., 1996, AJ, 112, 1415
- Jones, H. & Bland-Hawthorn, J., 1997, PASA, 14, 8
- Kennicutt, R. C., 1992, ApJS, 79, 255
- Kodama, T. & Arimoto N., 1997, A&A, 320, 41
- Kodama, T., 1997, Ph.D. Thesis, Univ. of Tokyo
- Kodama, T., Arimoto, N., Barger, A. J., & Aragón-Salamanca, A., 1998, A&A, 334, 99
- Köppen, J. & Arimoto, N., 1990, A&AS, 240, 22
- Lanzetta, K. M., Yahil, A., & Fernández-Soto, A., 1996, Nature, 381, 759
- Madau, P., Ferguson, H. C., Dickinson, M. E., Giavalisco, M., Steidel, C. C., & Fruchter, A., 1996, MNRAS, 283, 1388
- Marzke, R. O., Geller, M. J., Huchra, J. P., & Corwin Jr., H. G., 1994, AJ, 108, 437
- Marzke, R. O., da Costa, L. N., Pellegrini, P. S., Willmer, N. A., & Geller, M. J., 1998, astro-ph/9805218
- Mathis, J. S., 1990, ARA&A, 28, 37
- Metcalf, N, Shanks, T., Campos, A., Fong, R., & Gardner, J.P., 1996. Nature, 383, 236
- Mobasher, B., Rowan-Robinson, M., Georgakakis, A., & Eaton, N. 1996, MNRAS, 282, 7
- Nomoto, K., 1993, private communication
- Pickles, A. J. & van der Kruit, P. C., 1991, A&AS, 91, 1
- Salpeter, E. E., 1955, ApJ, 121, 161
- Sawicki, M. J., Lin, H., & Yee, H. K. C., 1997, AJ, 113, 1
- Schechter, P. L., 1976, ApJ, 203, 297
- Schmidt, M., 1959, ApJ, 129, 243
- Shimasaku, K. & Fukugita, M., 1998, ApJ, in press
- Simien, F. & de Vaucouleurs, G., 1986, ApJ, 302, 564
- Stanford, S. A., Eisenhardt, P. R. M., & Dickinson, M., 1995, ApJ, 450, 512
- Stanford, S. A., Eisenhardt, P. R. M., & Dickinson, M., 1998, ApJ, 492, 461
- Stanford, S. A., Elston, R., Eisenhardt, P. R., Spinrad, H., Stern, D., & Dey, A., 1997, AJ, 114, 2232
- Steidel, C. C., Adelberger, K. L., Dickinson, M., Giavalisco, M., Pettini, M., & Kellogg, M., 1998, ApJ, 492, 428
- Steidel, C. C., Giavalisco, M., Pettini, M., Dickinson, M., & Adelberger, K. L., 1996, ApJ, 462, 17
- Taylor, K., 1995, A&AS, 186, 4406
- Tinsley, B. M., 1980, Fundamentals of Cosmic Physics, Vol.5, p.287
- White III R.E., Keel W.C., & Conselice C.J., 1996, astro-ph/9608113
- Williams, R. E., et al., 1996, AJ, 112, 1335
- Worthey, G., 1994, ApJS, 95, 107
- Yamada, T., Tanaka, I., Aragón-Salamanca, A., Kodama, T., Ohta, K., & Arimoto, N., 1997, ApJ, 487, L125
- Yi, S., Demarque, P., & Oemler, Jr. A., 1997, ApJ, 486, 201
- Young, J. S. & Knezek, P. M., 1989, ApJ, 347, L55